PHOTONICS Research

Polarization independent high-speed spatial modulators based on an electro-optic polymer and silicon hybrid metasurface

XINYU SUN[1,2] **AND FENG QIU**[3,*]

[1]College of Optical Science and Engineering, Zhejiang University, Hangzhou 310027, China
[2]Institute of Advanced Technology, Westlake Institute for Advanced Study, Westlake University, Hangzhou 310024, China
[3]Hangzhou Institute for Advanced Study, University of Chinese Academy of Sciences, Hangzhou 310024, China
*Corresponding author: a-photonics@outlook.com

Received 28 September 2022; accepted 27 October 2022; posted 27 October 2022 (Doc. ID 476688); published 1 December 2022

Dynamical control of the constitutive properties of a light beam is important for many applications in photonics and is achieved with spatial light modulators (SLMs). Performances of the current demonstrations, such as liquid-crystal or micro-electrical mechanical SLMs, are typically limited by low (~kHz) switching speeds. Here, we report a high-speed SLM based on the electro-optic (EO) polymer and silicon hybrid metasurface. The specially configured metasurface can not only support a high-*Q* resonance and large "optical–electrical" overlap factor, but also overcome the challenge of polarization dependence in traditional EO modulators. Combined with the high EO coefficient of the polymer, a 400 MHz modulation with an RF driving source of 15 dBm has been observed in the proof-of-concept device near the wavelength of 1310 nm. The device with the desired merits of high speed, high efficiency, and micrometer size may provide new opportunities for high-speed smart-pixel imaging, free-space communication, and more.

https://doi.org/10.1364/PRJ.476688

1. INTRODUCTION

Spatial light modulators (SLMs) provide fine-grained real-time control of light in free space. Recently, there has been a dramatic increase in demand of high-speed SLMs to enable novel applications such as beam steering for LiDAR, fast free-space optical telecommunication, and biomedical imaging [1–5]. Current techniques rely mainly on employed liquid crystals [6,7], phase-transition materials [8,9], micro-electromechanical systems [10,11], and digital micro-mirror devices [12,13]. However, they suffer from intrinsic properties of material or device structure mechanisms, limiting the response time in the millisecond regime.

The electro-optic (EO) polymer possessing Pockels effect has shown unprecedented capabilities in developing high-speed modulators. EO polymer is intrinsically advantageous over its counter inorganic EO materials in many aspects, such as large EO coefficients $r_{33} > 100$ pm/V [14–17], high-speed EO response less than 10 fs [18], phase-only modulation, and great compatibility in directing substrates in systems [16,19]. EO polymer modulators based on optical waveguides have already enabled 100 Gbit/s operation and fJ/bit power consumption [20–22]. As a result, if EO polymer is applied in SLMs, it may promote high-speed modulation, low driving voltage, and relatively simple fabrication.

There are two fundamental challenges in realizing an EO polymer SLM: the ultra-short modulation path and polarization dependent performance [23]. Conventional waveguide-based EO polymer modulators are based on phase accumulation with light propagation in several millimeters to centimeters long waveguides, so an enough phase change of propagated light can be obtained even with a low driving voltage of several volts [24,25]. However, an SLM usually utilizes a top–bottom electrode structure (Fig. 1) with a sandwiched EO polymer [26–28]. The EO polymer acts as the modulating layer with a thickness of the order of the operating wavelength. Such an ultra-short modulation path will force the SLM to be driven with a high voltage to stimulate moderate modulation [28–30]. In addition, the maximum EO coefficient r_{33} of the EO polymer is achieved along the direction of the poling electric field [31–33]. Therefore, the polarization of the modulated light should be along the direction of the poling electric field [27], which leads to modulators with polarization dependent performance and narrows the range of potential applications.

To overcome these obstacles, we have designed and fabricated a polarization independent SLM that is able to support fast modulation in the near-infrared region. This device integrates EO polymer with the symmetry metasurface constructed by periodic Si square pillars. The EO polymer is sandwiched

2327-9125/22/122893-08 Journal © 2022 Chinese Laser Press

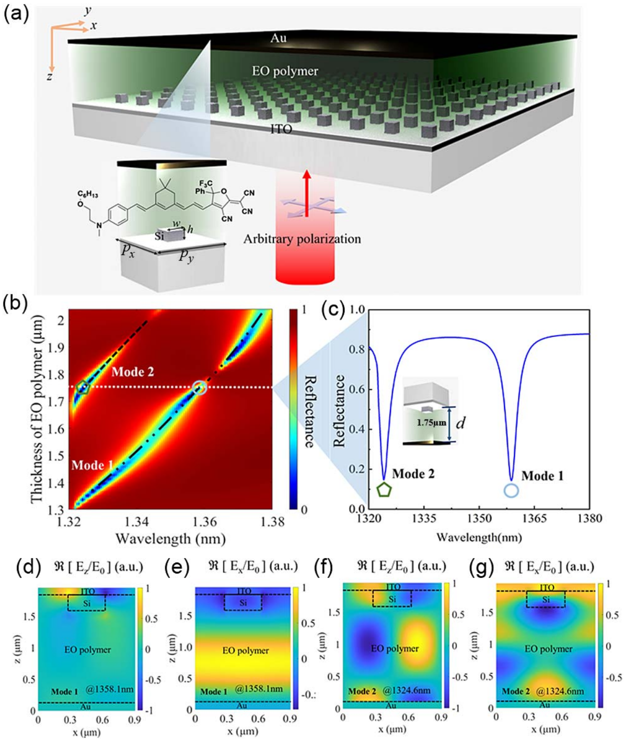

Fig. 1. (a) 3D illustration of the proposed structure. The structure consists of an Au back plane, EO polymer (structure of the used chromophore is shown inside), and a thin ITO film on the designed Si metasurface. Unit cell dimensions are: $w = 0.35$ μm, $h = 0.33$ μm, $P = p_x = p_y = 0.905$ μm. Thicknesses of ITO, Au back plane, and EO polymer are 0.1 μm, 0.1 μm, and 1.75 μm, respectively. (b) Simulated reflectance versus the working wavelength and EO polymer thickness. Horizontal dashed line indicates the optimized thickness of EO polymer of devices for high Q and large extinction ratio. (c) Reflective spectrum with the optimized EO polymer thickness. (d), (e) Spatial profile of the z component electric field $\mathcal{R}\,[E_z/E_0]$ and x component electric field $\mathcal{R}\,[E_x/E_0]$ at the resonant wavelength of 1358.1 nm (mode 1). (f), (g) Spatial profile of the z component electric field $\mathcal{R}\,[E_z/E_0]$ and x component electric field $\mathcal{R}\,[E_x/E_0]$ at the resonant wavelength of 1324.6 nm (mode 2).

directly between the top and bottom electrodes, thus significantly increasing the electric poling and modulating field applied on the EO polymer layer. The specially designed metasurface enables polarization independent modulation and confines most of the incident light in the active EO polymer layer. Combining all of these merits together, the fabricated modulator realized a modulating speed up to 400 MHz. To the best of our knowledge, it is the first polarization independent SLM in the near-infrared region with such high modulation speed.

2. ARCHITECTURE AND OPERATION PRINCIPLE

A schematic illustration of the proposed device is depicted in Fig. 1(a), where an Au/EO polymer/Si/ITO four-layer stack is built on a quartz substrate. In this configuration, the resonant wavelengths of the modulator are shifted under the applied driving voltage by means of the Pockels effect of the EO polymer. The Au and ITO layers serve as a pair of vertical electrodes for applying poling and driving voltage. The active layer EO polymer is sandwiched between the top Au electrode (100 nm thick) and bottom ITO (100 nm thick), so that a perpendicular electrical field E_{eo} is formed in the EO polymer under applied bias. The phase change $\Delta\varphi$ of the propagated light is expressed as [31,34]

$$\Delta\varphi = k_0 \Delta n L = \frac{1}{2} n^3 r_{33} \Gamma E_{\mathrm{eo}} k_0 L, \tag{1}$$

where k_0 is the vacuum wavenumber, Δn the change of refractive index induced by the EO effect, L the length of the modulation path, n the effective refractive index of the EO polymer, r_{33} the EO coefficient of the EO polymer, and Γ the overlap factor between the optical field and the electrical field E_{eo}. The EO material used in this work is a mixture of a 33 wt% chromophore [molecular structure shown in Fig. 1(a)] and a PMMA host polymer. Since the change of refractive index of EO polymer undergoes of the order of 10^{-4}–10^{-5} V^{-1} under applied bias and L is just several micrometers, a Si metasurface is designed resting on the bottom indium tin oxide (ITO) to construct a high-Q resonance for enhancing light–matter interactions [35]. The specially designed Si metasurface consists of periodic lattices of square pillars. All Si pillars have the same height h of 330 nm and width w of 350 nm. One unit of the periodic lattice has lattice constants of $P = p_x = p_y =$ 905 nm. This device is polarization independent, which arises from the geometric intrinsic symmetry of the designed Si metasurface [36,37]. The further parametric optimations are discussed in Appendix A to realize a higher Q-factor and a large extinction ratio.

As a plane-wave light is normally incident to the device as shown in Fig. 1(a), a series of guide mode resonant (GMR) modes may be excited in the EO polymer layer. The dominant resonance of the SLM is based on the GMR, which is one of the great candidates for making high Q-factor resonances [38,39]. Unlike metasurfaces that demonstrate Mie resonances or Huygens' surfaces [40–42], high-index Si nano-antennas work as 2D gratings, so that light can be coupled into the device. The propagation constant corresponding to the ith order diffracted wave of the grating is $\beta = k(-\frac{i\lambda}{P})$, where $k = \frac{2\pi}{\lambda}$, and λ is the free-space wavelength. The EO polymer layer acts as a slab waveguide that confines the coupled guided mode. When the wave vector of the guided mode matches that of the Si grating, the resonance can be excited. Tuning the thickness of the EO polymer would result in arbitrary control over the number, Q-factor, and resonance wavelength of the resonant modes. Figure 1(b) shows the simulated reflectance of the device with different EO polymer thicknesses d. It should be noted that the reflected spectra are independent of the polarization of the input light. Considering the spin-coating process for obtaining the EO polymer film, d is set from 1.3 to 2.2 μm. From Fig. 1(b), we can see that two resonance valleys emerge along well-defined curves (black dotted curves). When d is smaller than 1.65 μm, only resonant mode 1 is excited. As the EO polymer becomes thicker, we observe that mode 2 appears and two modes co-exist inside the SLM, which is coincident with the behavior of the guide mode in the pure slab waveguide (Appendix B). To realize resonances with high-Q values and

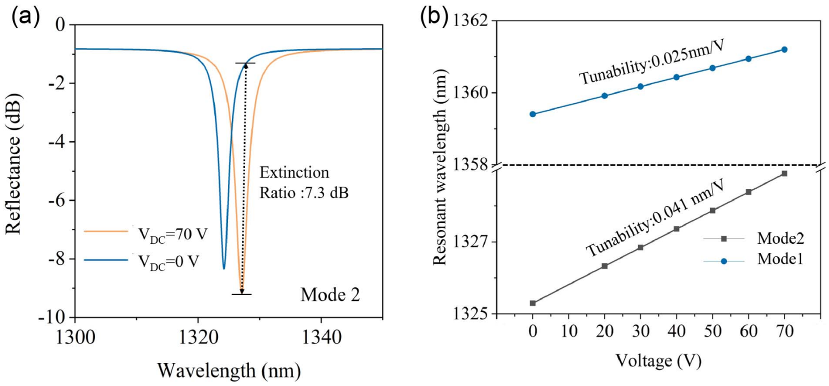

Fig. 2. (a) Simulated reflective spectrum with unbiased and 70 V voltage. (b) Shift of the resonance wavelength linearly fitted with the bias voltages of mode 1 and mode 2.

large extinction ratios, the optimal d is selected as 1.75 μm. Figure 1(c) shows the simulated reflective spectra of the two distinct resonant modes. The two resonances locate at wavelengths of 1358.1 nm with a Q-factor as 203 (mode 1) and 1324.6 nm with a Q-factor as 220 (mode 2).

Based on Eq. (1), we can also note that the overlap factor Γ is another important parameter to achieve efficient EO modulation. Since the device is poled and driven vertically, the dominant component of the resonant mode should be along z direction [43]. We have calculated the field distribution of both resonant modes. The plots of simulated optical field distributions of mode 1 and mode 2 are shown in Figs. 1(d)–1(g). For mode 1, the optical field is strongly concentrated within the EO polymer, but the x component of the optical field is dominant with little light in the z component [Figs. 1(d) and 1(e)]. In contrast, the optical field of mode 2 is confined in the EO polymer both vertically and laterally [Figs. 1(f) and 1(g)]. According to our calculations, approximately 56% light of mode 2 polarizes along z direction, which is beneficial to the low-voltage driving of the modulator. In this work, therefore, we choose mode 2 as the working mode to obtain high modulation efficiency.

Figure 2(a) exhibits the simulated reflected spectra of mode 2 without and with applied DC voltage. In the simulation, r_{33} of the EO polymer is set as 100 pm/V. From the spectra, the device holds an extinction ratio of around 7.3 dB and a negligible Q-factor change under different biases. The extinction ratio is defined as the reflectance difference of $R(0)$ and $R(V)$, where $R(V)$ is reflectance at driving voltage V, and $R(0)$ is the reflectance at 0 V. The tunability of the device is determined by calculating reflection as a function of resonance peak wavelength with the device biased at several DC voltages. As shown in Fig. 2(b), the calculated tunabilities of the device are 0.041 nm/V and 0.025 nm/V for mode 2 and mode 1, respectively. Thus, the tunability can be improved by more than 60% by skillfully designing the optical mode.

3. EXPERIMENTAL RESULTS

A. Polarization Independent Resonance

First, we characterize the resonant behavior of the SLM under different polarizations via the setup as schematically shown in Fig. 3(a). A supercontinuum laser was used as the light source, and its polarization was controlled by a polarizer. The scanning electron microscopy image of the device before spin-coating EO polymer is shown in Fig. 3(b). From the measured reflected spectra without applied voltage in Fig. 3(c), we can observe that the resonant wavelengths and the line shapes of the spectra are almost identical when the polarization of the incident light varies from 0° to 90°. All reflected spectra exhibit two deep

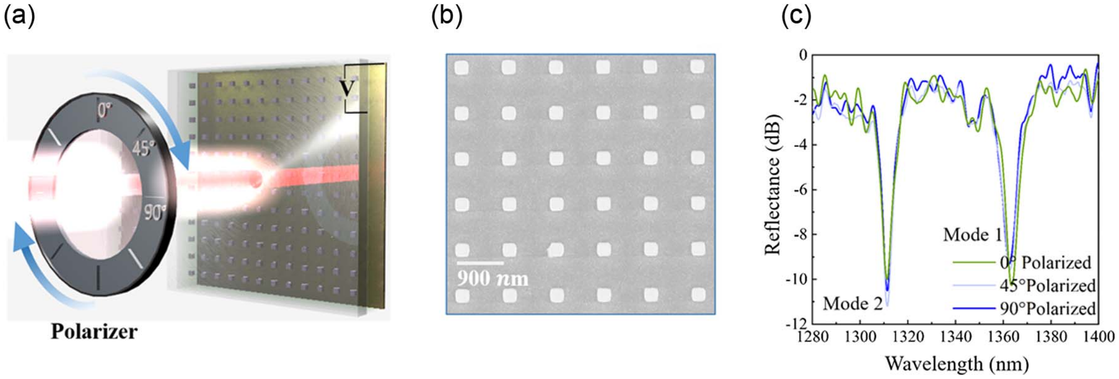

Fig. 3. (a) Schematic of the experimental process to demonstrate the polarization independence property of the modulators. (b) Scanning electron microscopy images of Si square pillars on ITO layer before spin-coating EO polymer. (c) Resonant spectra under incident light with different polarization states (without applied bias).

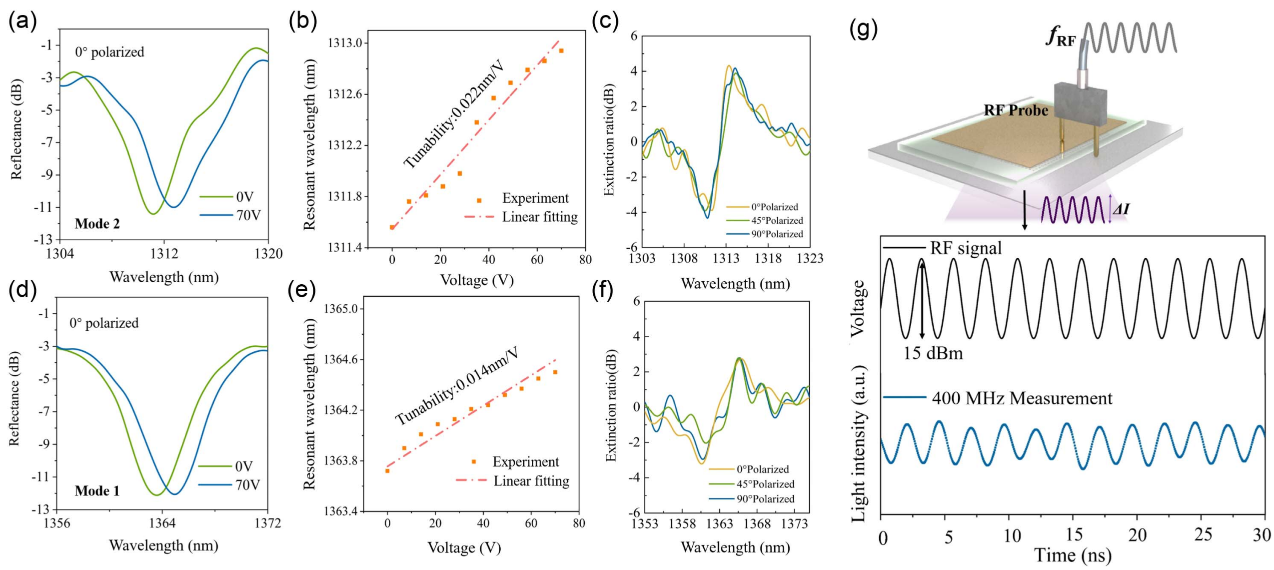

Fig. 4. Measured reflective spectra, tunability, and extinction ratio under different polarizations: (a)–(c) mode 2; (d)–(f) mode 1. (g) Measured high-speed reflectance modulation (blue) upon 15 dBm RF signal (black) with operation speed of 400 MHz.

resonant dips, corresponding to mode 1 (1362.4 nm) and mode 2 (1311.5 nm) with Q-factors of 151 and 153, respectively. The above results indicate that our device circumvents the inherent sensitivity of EO polymer modulators to incident polarization. The slight difference from the simulated spectrum can be attributed to several factors, such as the Si metasurface being imperfect (dimensional, roughness) and the thickness of the EO polymer.

B. DC and High-Speed RF Modulation

The EO property of the SLM was determined by measuring reflection as a function of resonant wavelength with the device biased at several DC voltages (measurement setup in Appendix C). Figure 4(a) shows the measured reflectance spectra of mode 2 with an obvious shift of 1.54 nm under a voltage bias of 70 V. With voltage varying from 0 to 70 V, the resonant wavelength shift is almost linear as shown in Fig. 4(b) resulting from the Pockels effect of the EO polymer. By linear fitting, the tunability is extracted as 0.022 nm/V. Based on Eq. (1) and the tunability, the calculated in-device r_{33} of the EO polymer is 51 pm/V. Figure 4(c) exhibits the extinction ratio of the modulated light at different wavelengths at the applied voltage of 70 V. It can be observed that the EO modulation works for normally incident light of any polarization, and the largest modulating extinction ratio is around 4.5 dB at the wavelength of 1312.8 nm. For comparison, we also measured the tunability and largest modulating extinction ratio of mode 1, which are 0.014 nm/V and 2.7 dB, respectively. The outstanding behaviors of mode 2 over mode 1 are in good agreement with numerical simulations.

For verification of the device as the optical intensity modulator, we fixed the input laser wavelength at the resonance point and applied the RF driving source with a $V_{\text{p-p}} \sim 1.3$ V. The RF signal from an RF generator was applied to the electrodes via electrical probes, and an amplified photodetector was used to detect the temporal changes. As shown in Fig. 4(g), the input electric signal (black) and the output temporal optical response (blue) were monitored by an oscilloscope. The device exhibits clear modulation up to 400 MHz with a polarization independent characteristic. The modulation speed of an EO resonator modulator is determined by the cavity photo lifetime τ and the capacitive RC-delay time (R is the resistance and C is the capacitance) [22]. τ is given as $\tau = \lambda Q/(2\pi c)$, where c is the light speed in vacuum, and Q is the quality factor. For our SLM, the Q-factor is 153, corresponding to a modulation speed of 1.49 THz. Therefore, the modulation speed of our device should be limited by the RC-delay time expressed as $1/(2\pi RC)$. For our EO polymer cavity concept, the size of the capacitor can be reduced to match the light spot area to lower the capacitance, which would yield capacitance as low as 40 fF (area = 50 μm × 50 μm). Such a small capacitance can enable modulation speed up to 7.9 GHz in future work [44].

4. CONCLUSION

In conclusion, we have demonstrated a high-speed SLM operating around 1310 nm based on the EO polymer and Si hyrbid metasurface. The optimized metasurface utilizes intrinsically symmetrical geometry to achieve polarization independent modulation, while maintaining relatively high-Q resonance. Combined with the large EO coefficient and fast response of EO polymer, the SLM shows an extinction ratio of 4.5 dB at 70 V bias, tunability of 0.022 nm/V, and clear fast modulation at 400 MHz. The modulation speed can be increased to 7.9 GHz via further improving the capacity of the device. We believe that our proposed device concept could lead to advances in free-space optics and micro/nano photonics.

5. EXPERIMENT

A. Device Fabrication

The proposed device was fabricated via standard thin film deposition processes and E-beam lithography (EBL) techniques.

Each layer was stacked in order from bottom (ITO) to top (Au). First, we deposited a 100 nm ITO layer on a quartz substrate using RF sputtering in Ar–O_2 plasma. The film was then annealed to modify the permittivity of ITO, which was verified by using spectroscopic ellipsometry. The pattern was fabricated on a 0.33 μm thick Si thin film prepared by using plasma-enhanced chemical vapor deposition (PECVD). Afterwards, the Si pattern was performed by EBL and development (ma-N 2405 as the photosensitive film and ma-D 525 as the developing agent). Etching was carried out via inductively coupled plasma (ICP). Subsequently, the device was cleaned with an O_2 plasma treatment. We spin-coated EO polymer on the device and baked it over 12 h. Finally, the 100 nm thick Au electrode layer used thermal evaporation as the deposition mechanism (the rate was 0.4 A s^{-1}).

B. Simulations

We used the commercial electromagnetic simulator established on the finite-difference time-domain method to perform numerical calculations (Lumerical FDTD). The boundary conditions are a perfectly matched layer along *z* direction and periodic boundary along *x* and *y* directions. The properties of gold were adopted from the handbook [45]. For other materials, they were extracted experimentally through spectroscopic ellipsometry measurements. The eigenfrequency calculation was carried out by using the commercial finite element method (COMSOL Multiphysics).

6. COMPARISON WITH PRIOR ARTS

In Table 1, the EO polymer and Si hybrid metasurface SLM is compared with prior works. In this discussion, we restrict ourselves to devices working in the region of electrically driven SLMs.

Table 1. Comparison of Different Types of Electrically Driven SLMs

Approach	Material	Speed	Polarization Independence	V_{p-p}	Reference
Phase transition	Liquid crystal	–	No	70 V	[6]
	VO_2	<300 kHz	No	–	[8]
	GLS	<50 kHz	No	~45 V	[46]
Carrier doping	Graphene	1.2 GHz	No	–	[44]
	ITO	<1 MHz	No	2 V	[47]
		10 MHz	No	2.5 V	[48]
Pockels effect	$LiNbO_3$	<1 MHz	No	24 V	[29]
		2.5 MHz	Yes	1 V	[30]
	EO polymer	5 MHz	No	10 V	[28]
		50 MHz	No	–	[23]
Pockels effect	**This work**	**400 MHz**	**Yes**	**1.3 V**	**Ours**

APPENDIX A: OPTIMIZATION PARAMETERS OF Si SQUARE METASURFACES

To optimize the performance of resonance modes, including *Q*-factor (=λ_0/FWHM, where λ_0 is the resonant wavelength and FWHM the full width at half maxima) and modulation depth, we have investigated the parametric analysis on the width and period lattice constants of Si square particles. To improve modulation efficiency and achieve a low driving voltage, the optimized structure should provide resonance with FWHM as small as possible. To achieve a large modulation depth, the depth of the resonance dip should be as large as possible. As depicted in Fig. 5, we compare the performance of the two modes as the width of Si square particles varies from 0.33 and 0.37 μm, and the period varies from 0.89 to 0.92 μm. In these ranges, the resonances would localize at wavelengths of the O band. Periods of 0.89 and 0.92 μm result in either the largest FWHM or smallest resonant depth for mode 1 and mode 2, respectively. The choice of width is also the trade-off result between the increased FWHM and the decrease of the depth of the resonant dip with larger width. Thus, we finally choose the width of 0.35 μm and period of 0.905 μm as the optimized configuration, because they represent the best compromise between the FWHM and the depth of the resonance dips.

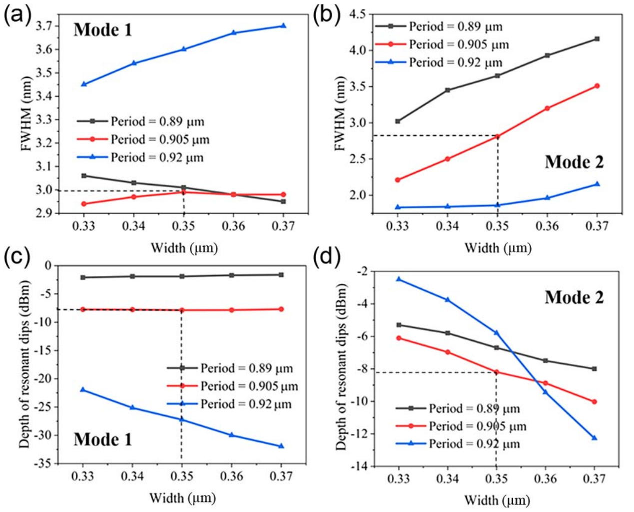

Fig. 5. (a)–(d) Parametric analysis on the width and period of Si square particles. The black dotted line represents the optimized configuration used in the final discussion with width of 0.35 μm and period of 0.905 μm.

APPENDIX B: EIGENFREQUENCY OF GUIDED MODES

When the high-order wave ($i = 1$ and/or –1) from the grating can be phase matched to the guided mode of the slab waveguide, the resonance is excited. By solving the eigenfrequency of the pure slab waveguide with β of the diffracted wave from the grating, the approximate guide mode resonances can be found. We simplified the device to a four-layer (quartz/ITO/EO polymer/Au) structure and calculated eigenfrequency with different thicknesses of EO polymer [Fig. 6(a)]. When a thicker waveguide (EO polymer) is applied, multiple modes can be excited simultaneously. Figure 6(b) shows the simulated spectrum from the SLM with different thicknesses of EO polymer, where these three modes demonstrate similar trends to calculated results.

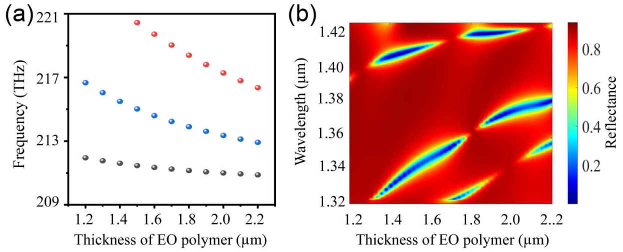

Fig. 6. (a) Calculated eigenfrequency of different modes with different thicknesses of EO polymer. (b) Simulated reflectance with different thicknesses of EO polymer.

APPENDIX C: REFLECTION SPECTRUM SETUP AND HIGH-FREQUENCY RF SIGNAL RESPONSE MEASUREMENTS

The reflected spectra of the device were measured by using a home-built optical system as schematically shown in Fig. 7. A supercontinuum laser (SC5, Yangtze Soton Laser) was used as the light source. The light was first collimated by a lens (L) and iris (I). A polarizer (P) was inserted after the iris to control the input light polarization. After passing a 50:50 beam splitter (BS), the light refracted by a mirror was finally focused by another lens onto the device. The lens inserted between the mirror (M) and the sample is to control the light spot that projects onto the sample. The reflected light from the device under test (DUT) was diverted by the BS and sent to an optical spectrum analyzer (OSA) (AQ6370D, Yokogawa).

The measurement setup for the high-frequency RF signal response is shown in Fig. 8. First, the wavelength of the output light from a tunable laser (TSL-510, Santec) is fixed at the operating wavelength. To characterize the RF response of our modulator, RF signal from the RF signal generator (SMT03, Rohde & Schwarz) with power of 15 dBm and frequency ranging from 100 to 400 MHz is applied to the electrodes of the device through microwave probes. The real-time change of the reflected light was detected by a high-speed InGaAs amplified photodetector (APRM-KY). An oscilloscope displays waveforms of the optical signal and the RF signal through multi-channels.

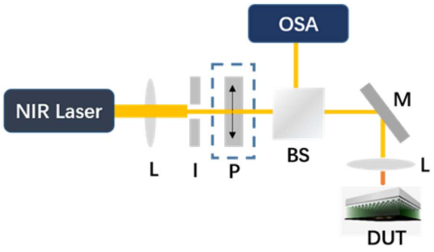

Fig. 7. Custom-built optical system for measuring the reflectance spectra of the device.

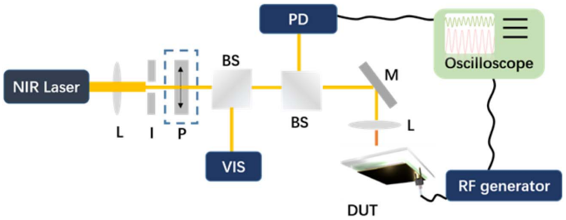

Fig. 8. Custom-built optical system and high-frequency RF modulation measurement system.

APPENDIX D: OPTICAL CHARACTERISTICS OF THE ITO FILM

The ITO films in our experiment were deposited by RF magnetron sputtering. To obtain high-Q resonance, we need to reduce the absorption loss of ITO. The optical absorbance of ITO is varied by controlling the ratio of Ar and O_2 flow rates during deposition. We finally adjust the flow rates of O_2 and Ar as 9 and 100 sccm (standard cubic centimeters per minute), respectively. The measured refractive index of ITO and the absorption coefficient are shown in Fig. 9.

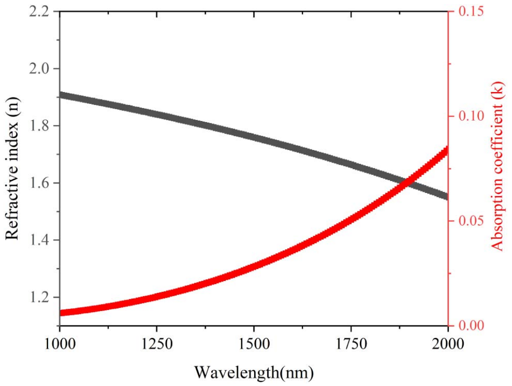

Fig. 9. Measured data of refractive index and absorption coefficient of ITO.

Funding. National Natural Science Foundation of China (501100001809).

Disclosures. The authors declare no conflicts of interest.

Data Availability. Data underlying the results presented in this paper are not publicly available at this time but may be obtained from the authors upon reasonable request.

REFERENCES

1. N. Savage, "Digital spatial light modulators," Nat. Photonics **3**, 170–172 (2009).
2. A. Smolyaninov, A. El Amili, F. Vallini, S. Pappert, and Y. Fainman, "Programmable plasmonic phase modulation of free-space wavefronts at gigahertz rates," Nat. Photonics **13**, 431–435 (2019).
3. J. S. Ahearn, M. H. Weiler, S. B. Adams, T. P. McElwain, A. Stark, L. DePaulis, A. L. Sarafinas, T. Hongsmatip, R. J. Martin, and B. Lane, "Multiple quantum well (MQW) spatial light modulators (SLMs) for optical data processing and beam steering," Proc. SPIE **4457**, 43–53 (2001).
4. B. Schwarz, "Mapping the world in 3D," Nat. Photonics **4**, 429–430 (2010).

5. S.-Q. Li, X. Xu, R. Maruthiyodan Veetil, V. Valuckas, R. Paniagua-Domínguez, and A. I. Kuznetsov, "Phase-only transmissive spatial light modulator based on tunable dielectric metasurface," Science **364**, 1087–1090 (2019).
6. A. Komar, Z. Fang, J. Bohn, J. Sautter, M. Decker, A. Miroshnichenko, T. Pertsch, I. Brener, Y. S. Kivshar, I. Staude, and D. N. Neshev, "Electrically tunable all-dielectric optical metasurfaces based on liquid crystals," Appl. Phys. Lett. **110**, 071109 (2017).
7. H. Mbarak, S. M. Hamidi, E. Mohajerani, and Y. Zaatar, "Electrically driven flexible 2D plasmonic structure based on a nematic liquid crystal," J. Phys. D **52**, 415106 (2019).
8. Z. Zhu, P. G. Evans, R. F. Haglund, and J. G. Valentine, "Dynamically reconfigurable metadevice employing nanostructured phase-change materials," Nano Lett. **17**, 4881–4885 (2017).
9. Y. Kim, P. C. Wu, R. Sokhoyan, K. Mauser, R. Glaudell, G. Kafaie Shirmanesh, and H. A. Atwater, "Phase modulation with electrically tunable vanadium dioxide phase-change metasurfaces," Nano Lett. **19**, 3961–3968 (2019).
10. E. Arbabi, A. Arbabi, S. M. Kamali, Y. Horie, M. Faraji-Dana, and A. Faraon, "MEMS-tunable dielectric metasurface lens," Nat. Commun. **9**, 812 (2018).
11. M. Manjappa, P. Pitchappa, N. Singh, N. Wang, N. I. Zheludev, C. Lee, and R. Singh, "Reconfigurable MEMS Fano metasurfaces with multiple-input–output states for logic operations at terahertz frequencies," Nat. Commun. **9**, 4056 (2018).
12. D. Dudley, W. M. Duncan, and J. Slaughter, "Emerging digital micromirror device (DMD) applications," Proc. SPIE **4985**, 14–25 (2003).
13. S. Turtaev, I. T. Leite, K. J. Mitchell, M. J. Padgett, D. B. Phillips, and T. Čižmár, "Comparison of nematic liquid-crystal and DMD based spatial light modulation in complex photonics," Opt. Express **25**, 29874–29884 (2017).
14. Y. Enami, C. T. Derose, D. Mathine, C. Loychik, C. Greenlee, R. A. Norwood, T. D. Kim, J. Luo, Y. Tian, A. K.-Y. Jen, and N. Peyghambarian, "Hybrid polymer/sol–gel waveguide modulators with exceptionally large electro–optic coefficients," Nat. Photonics **1**, 180–185 (2007).
15. D. L. Elder, S. J. Benight, J. Song, B. H. Robinson, and L. R. Dalton, "Matrix-assisted poling of monolithic bridge-disubstituted organic NLO chromophores," Chem. Mater. **26**, 872–874 (2014).
16. T.-D. Kim, J. Luo, J.-W. Ka, S. Hau, Y. Tian, Z. Shi, N. M. Tucker, S.-H. Jang, J.-W. Kang, and A. K.-Y. Jen, "Ultralarge and thermally stable electro-optic activities from Diels–Alder crosslinkable polymers containing binary chromophore systems," Adv. Mater. **18**, 3038–3042 (2006).
17. H. Xu, D. L. Elder, L. E. Johnson, Y. de Coene, S. R. Hammond, W. Vander Ghinst, K. Clays, L. R. Dalton, and B. H. Robinson, "Electro-optic activity in excess of 1000 pm V^{-1} achieved via theory-guided organic chromophore design," Adv. Mater. **33**, 2104174 (2021).
18. F. Qiu and Y. Han, "Electro-optic polymer ring resonator modulators [Invited]," Chin. Opt. Lett. **19**, 041301 (2021).
19. S. J. Benight, D. H. Bale, B. C. Olbricht, and L. R. Dalton, "Organic electro-optics: understanding material structure/function relationships and device fabrication issues," J. Mater. Chem. **19**, 7466–7475 (2009).
20. S. Koeber, R. Palmer, M. Lauermann, W. Heni, D. L. Elder, D. Korn, M. Woessner, L. Alloatti, S. Koenig, P. C. Schindler, H. Yu, W. Bogaerts, L. R. Dalton, W. Freude, J. Leuthold, and C. Koos, "Femtojoule electro-optic modulation using a silicon–organic hybrid device," Light Sci. Appl. **4**, e255 (2015).
21. M. Burla, C. Hoessbacher, W. Heni, C. Haffner, Y. Fedoryshyn, D. Werner, T. Watanabe, H. Massler, D. L. Elder, L. R. Dalton, and J. Leuthold, "500 GHz plasmonic Mach-Zehnder modulator enabling sub-THz microwave photonics," APL Photon. **4**, 056106 (2019).
22. C. Haffner, D. Chelladurai, Y. Fedoryshyn, A. Josten, B. Baeuerle, W. Heni, T. Watanabe, T. Cui, B. Cheng, S. Saha, D. L. Elder, L. R. Dalton, A. Boltasseva, V. M. Shalaev, N. Kinsey, and J. Leuthold, "Low-loss plasmon-assisted electro-optic modulator," Nature **556**, 483–486 (2018).
23. I.-C. Benea-Chelmus, M. L. Meretska, D. L. Elder, M. Tamagnone, L. R. Dalton, and F. Capasso, "Electro-optic spatial light modulator from an engineered organic layer," Nat. Commun. **12**, 5928 (2021).
24. C. Kieninger, C. Kieninger, C. Kieninger, Y. Kutuvantavida, Y. Kutuvantavida, D. L. Elder, S. Wolf, H. Zwickel, M. Blaicher, J. N. Kemal, M. Lauermann, S. Randel, W. Freude, L. R. Dalton, C. Koos, and C. Koos, "Ultra-high electro-optic activity demonstrated in a silicon-organic hybrid modulator," Optica **5**, 739–748 (2018).
25. H. Sato, H. Miura, F. Qiu, A. M. Spring, T. Kashino, T. Kikuchi, M. Ozawa, H. Nawata, K. Odoi, and S. Yokoyama, "Low driving voltage Mach-Zehnder interference modulator constructed from an electro-optic polymer on ultra-thin silicon with a broadband operation," Opt. Express **25**, 768–775 (2017).
26. X. Sun, H. Yu, N. Deng, D. Ban, G. Liu, and F. Qiu, "Electro-optic polymer and silicon nitride hybrid spatial light modulators based on a metasurface," Opt. Express **29**, 25543–25551 (2021).
27. X. Sun, G. Liu, H. Yu, D. Ban, N. Deng, and F. Qiu, "Design and theoretical characterization of high speed metasurface modulators based on electro-optic polymer," Opt. Express **29**, 9207–9216 (2021).
28. J. Zhang, Y. Kosugi, A. Otomo, Y.-L. Ho, J.-J. Delaunay, Y. Nakano, and T. Tanemura, "Electrical tuning of metal-insulator-metal metasurface with electro-optic polymer," Appl. Phys. Lett. **113**, 231102 (2018).
29. A. Weiss, C. Frydendahl, J. Bar-David, R. Zektzer, E. Edrei, J. Engelberg, N. Mazurski, B. Desiatov, and U. Levy, "Tunable metasurface using thin-film lithium niobate in the telecom regime," ACS Photon. **9**, 605–612 (2022).
30. H. Weigand, V. V. Vogler-Neuling, M. R. Escalé, D. Pohl, F. U. Richter, A. Karvounis, F. Timpu, and R. Grange, "Enhanced electro-optic modulation in resonant metasurfaces of lithium niobate," ACS Photon. **8**, 3004–3009 (2021).
31. J.-M. Brosi, C. Koos, L. C. Andreani, M. Waldow, J. Leuthold, and W. Freude, "High-speed low-voltage electro-optic modulator with a polymer-infiltrated silicon photonic crystal waveguide," Opt. Express **16**, 4177–4191 (2008).
32. J. J. Wolff and R. Wortmann, "Organic materials for second-order nonlinear optics," in *Advances in Physical Organic Chemistry*, D. Bethell, ed. (Academic, 1999), Vol. **32**, pp. 121–217.
33. P. M. Lundquist, M. Jurich, J.-F. Wang, H. Zhou, T. J. Marks, and G. K. Wong, "Electro-optical characterization of poled-polymer films in transmission," Appl. Phys. Lett. **69**, 901–903 (1996).
34. G.-W. Lu, J. Hong, F. Qiu, A. M. Spring, T. Kashino, J. Oshima, M. Ozawa, H. Nawata, and S. Yokoyama, "High-temperature-resistant silicon-polymer hybrid modulator operating at up to 200 Gbit s^{-1} for energy-efficient datacentres and harsh-environment applications," Nat. Commun. **11**, 4224 (2020).
35. S. Joseph, S. Sarkar, S. Khan, and J. Joseph, "Exploring the optical bound state in the continuum in a dielectric grating coupled plasmonic hybrid system," Adv. Opt. Mater. **9**, 2001895 (2021).
36. M.-C. Luo, F.-F. Ren, N. Gagrani, K. Qiu, Q. Wang, L. Yu, J. Ye, F. Yan, R. Zhang, H. H. Tan, C. Jagadish, and X. Ji, "Polarization-independent indium phosphide nanowire photodetectors," Adv. Opt. Mater. **8**, 2000514 (2020).
37. W. Zhou, K. Li, C. Song, P. Hao, M. Chi, M. Yu, and Y. Wu, "Polarization-independent and omnidirectional nearly perfect absorber with ultra-thin 2D subwavelength metal grating in the visible region," Opt. Express **23**, A413–A418 (2015).
38. S. S. Wang and R. Magnusson, "Theory and applications of guided-mode resonance filters," Appl. Opt. **32**, 2606–2613 (1993).
39. G. Quaranta, G. Basset, O. J. F. Martin, and B. Gallinet, "Recent advances in resonant waveguide gratings," Laser Photon. Rev. **12**, 1800017 (2018).
40. C. Liu, L. Chen, T. Wu, Y. Liu, J. Li, Y. Wang, Z. Yu, H. Ye, and L. Yu, "All-dielectric three-element transmissive Huygens' metasurface performing anomalous refraction," Photon. Res. **7**, 1501–1510 (2019).
41. M. Decker, I. Staude, M. Falkner, J. Dominguez, D. N. Neshev, I. Brener, T. Pertsch, and Y. S. Kivshar, "High-efficiency dielectric Huygens' surfaces," Adv. Opt. Mater. **3**, 813–820 (2015).
42. Y.-T. Lin, A. Hassanfiroozi, W.-R. Jiang, M.-Y. Liao, W.-J. Lee, and P. C. Wu, "Photoluminescence enhancement with all-dielectric coherent metasurfaces," Nanophotonics **11**, 2701–2709 (2022).

43. L. R. Dalton, S. J. Benight, L. E. Johnson, D. B. Knorr, I. Kosilkin, B. E. Eichinger, B. H. Robinson, A. K.-Y. Jen, and R. M. Overney, "Systematic nanoengineering of soft matter organic electro-optic materials," Chem. Mater. **23**, 430–445 (2011).
44. Y. Gao, R.-J. Shiue, X. Gan, L. Li, C. Peng, I. Meric, L. Wang, A. Szep, D. Walker, J. Hone, and D. Englund, "High-speed electro-optic modulator integrated with graphene-boron nitride heterostructure and photonic crystal nanocavity," Nano Lett. **15**, 2001–2005 (2015).
45. J. F. Shackelford, Y.-H. Han, S. Kim, and S.-H. Kwon, *CRC Materials Science and Engineering Handbook* (Routledge Handbooks Online, 2015).
46. Z. L. Sámson, K. F. MacDonald, F. De Angelis, B. Gholipour, K. Knight, C. C. Huang, E. Di Fabrizio, D. W. Hewak, and N. I. Zheludev, "Metamaterial electro-optic switch of nanoscale thickness," Appl. Phys. Lett. **96**, 143105 (2010).
47. Y. Lee, J. Yun, S. Kim, M. Seo, S. In, H. Jeong, S. Lee, N. Park, T. D. Chung, and B. Lee, "High-speed transmission control in gate-tunable metasurfaces using hybrid plasmonic waveguide mode," Adv. Opt. Mater. **8**, 2001256 (2020).
48. Y.-W. Huang, H. W. H. Lee, R. Sokhoyan, R. A. Pala, K. Thyagarajan, S. Han, D. P. Tsai, and H. A. Atwater, "Gate-tunable conducting oxide metasurfaces," Nano Lett. **16**, 5319–5325 (2016).